Available online at www.sciencedirect.com

ScienceDirect

Journal of Sound and Vibration 322 (2009) 264–281

JOURNAL OF SOUND AND VIBRATION

www.elsevier.com/locate/jsvi

A boundary element extension of Curle's analogy for non-compact geometries at low-Mach numbers

C. Schram*

LMS International, Interleuvenlaan 68, Researchpark Haasrode Z1, 3001 Leuven, Belgium

Received 10 March 2008; received in revised form 16 September 2008; accepted 5 November 2008
Handling Editor: C.L. Morfey
Available online 25 December 2008

Abstract

The aeroacoustic analogy derived by Curle for the prediction of the sound resulting from turbulence/body interactions has proved quite powerful for low Helmholtz numbers, i.e. when the interaction region is acoustically compact. In such case, incompressible flow modeling can be used to obtain the source field used as the input of the analogy. It was, however, shown in a previous paper that Curle's analogy can yield erroneous results for non-compact cases, when an incompressible flow model is adopted. Yet, at low-Mach numbers, incompressible flow modeling can be substantially more efficient than compressible simulations, due to the stiffness issues faced by the latter.

The present work focuses on the derivation of a method combining Curle's analogy with a boundary element method (BEM), in order to compensate for the weaknesses of the traditional approach at high Helmholtz numbers. The validation of this method is performed by application to a generic test case: the spinning of two vortex filaments in an infinite two-dimensional duct. This flow model is amenable to a nearly exact derivation by an incompressible vortex model. Moreover, the acoustic field can also be obtained very accurately using the tailored Green's function based on the duct modes, providing a reference solution to validate our numerical approach.

The sound field predicted using the BEM/Curle approach shows excellent agreement with the reference solution based on the tailored Green's function, thereby validating the general principle of BEM/Curle method and its numerical implementation.

1. Introduction

Modern aeroacoustic theory began about 50 years ago, triggered by the noise levels emitted by aeroengines, which were dominated by the high-speed jets at that time. Flow-induced noise has since become a concern in many other low-Mach number fields, such as automotive, high-speed trains and domestic appliances. A popular predictive approach to aeroacoustic problems is based on the distinction between noise generation and noise propagation mechanisms. This concept led Lighthill [1] to formulate his celebrated acoustical analogy for jet noise in the early 1950s. It was shown that the flow mechanisms responsible for sound radiation could be expressed in the form of equivalent sources in a uniform medium at rest, chosen as representative of

---

*Tel.: +32 16 384348; fax: +32 16 384350.
E-mail address: christophe.schram@lms.be

0022-460X/$ - see front matter © 2008 Elsevier Ltd. All rights reserved.
doi:10.1016/j.jsv.2008.11.011

the propagation region surrounding the listener. The concept of equivalent sources has proven quite powerful for low-Mach number applications. Curle [2] extended Lighthill's analogy to account for turbulence–body interaction and introduced a corresponding additional source mechanism that involves the reaction force exerted by the body on the surrounding fluid, equivalent to an acoustic dipole. Ffowcs Williams and Hawkings generalized Curle's analogy even further to account for body motion and the resulting Doppler effects.

These methods were applied with success to numerous cases, many of these being exterior problems. In the present work we are concerned with the noise generated by confined flows and its propagation within the ducting. The problem of aerodynamic sound generation in pipes was considered, following the aeroacoustic analogy, by Davies and Ffowcs Williams [3]. They showed that the acoustic efficiency of turbulence within a straight infinite duct varies with frequency, from a dipole-like behavior below the cut-off frequency to a free-field quadrupolar efficiency as soon as a few transverse modes are cut-on. Other studies related to internal aeroacoustics have focused on predicting the noise generated by duct geometrical discontinuities in relatively simple duct configurations (diaphragms, vanes, elbows, contractions/expansions) [4,5].

Low frequencies are often considered, which presents two significant advantages. Firstly, the source being acoustically compact, it can be modeled by a point source. Secondly, for frequencies below the duct cut-off, one-dimensional Green's functions can be employed to describe the acoustic propagation. However, in many industrial designs, discontinuities in duct systems are avoided whenever possible to minimize pressure losses due to flow separation. Furthermore the spectrum of interest extends often beyond the transverse cut-off frequency, up to several kHz.

Two steps are involved in the acoustic prediction: (i) describing the in-duct noise generation with adequate accuracy; (ii) propagating the emitted noise throughout the duct system, over a certain number of wavelengths, at frequencies high enough for transverse modes to be cut-on. We are considering in particular low-Mach applications related to heating, ventilating and air-conditioning (HVAC) systems, automotive exhausts (mufflers), and general fluid distribution pipings in process industries. The fact that the sources are distributed over non-compact distances gives rise to difficulties that are related to the assumption of compactness of the source region that is more or less implicit in the derivation of classic analogies. One of the consequences of non-compactness is the difficult discrimination between sound production and scattering effects, and is the focus of the present work.

Formally, the pressure fluctuation that is involved in the dipole source term of Curle's analogy accounts for any deviation from the reference pressure in the propagation region. Although the derivation of Curle's analogy does not make any formal assumption on the nature of the mechanisms causing the pressure variations, some care must be taken when interpreting these fluctuations as equivalent dipoles when the source region is non-compact. In such cases, the pressure fluctuations at the surface bounding the source region do not only account for hydrodynamic processes, but also for acoustic scattering, and the latter component has to be computed in some way and added to the hydrodynamic component in order to obtain correct results at the listener in the far field. This correction step is not needed in Curle's analogy, on the grounds that the acoustic component is irrelevant for a compact body. This was demonstrated by Gloerfelt et al. [6], who obtained an accurate prediction of the sound field produced by a cylinder in cross-flow, described by an incompressible flow model, at the vortex shedding frequency for which the cylinder diameter is acoustically compact. In contrast, using an incompressible flow model for a non-compact configuration can yield quite erroneous results, as was shown by Schram et al. [7].

A further remark is that while compressible flow simulations can theoretically capture acoustic propagation using high-order schemes with low dissipation and dispersion, the numerical cost associated with these methods is still prohibitive for many industrial purposes. Our purpose is to develop a numerical method for the determination of the acoustic scattering that is lacking using an incompressible flow model, in order to extend the applicability of Curle's analogy for non-compact configurations. It must be noted that the approach which is proposed in this paper is not aimed at correcting the flow itself, as would be necessary in cases where the acoustic field is large enough to couple strongly with the flow field. The aim is here to address low-Mach numbers, non-resonant applications in which the flow is responsible for, but not affected by the noise production. As a counter-example, important flow-acoustic back-reaction over non-compact distances occurs when a high-speed train enters a tunnel fitted with slotted hoods. Howe [8] showed that compactness effects can also be important in such applications, and must be explicitly accounted for in the modeling of the wave field.

A boundary element method (BEM) is applied in this work to numerically model non-compactness effects. The BEM approach consists of a discretization of the boundary integral solution of the Helmholtz equation, assuming a free-field Green's function for the calculation of the acoustic field at the listener position. It presents three main advantages, for our purpose, over the finite element method (FEM) [9]: (i) the meshing effort is lower, especially for geometries of industrial relevance; (ii) the FEM approach is affected by dispersion errors, while the BEM technique is not; (iii) the Sommerfeld radiation condition is naturally enforced, while sophisticated numerical techniques (e.g. infinite elements, perfectly matched layers) have to be implemented in an FEM context to obtain accurate free-field boundary conditions. Finally, its formal derivation is very similar to the one of Curle's analogy, providing a natural framework for our purpose. A similar boundary element approach has been followed by Takaishi et al. [10] to obtain a numerical Green's function for non-compact configurations.

The paper is organized as follows. The derivation of Curle's analogy is reproduced in Section 2, and the derivation of a BEM variant of Curle's analogy is detailed in Section 3. In order to validate the concept and implementation of the BEM/Curle method, a simple two-dimensional test case is considered in this work: the spinning of two vortex filaments in an infinite straight duct. The acoustic results obtained using the BEM/Curle method are compared to those obtained using a tailored Green's function in Section 4. Conclusions are drawn in Section 5.

2. Curle's analogy: reminder

Upon definition of a reference thermodynamic state (ρ_0, p_0) uniform in time and space in a propagation region, Lighthill's analogy describes the propagation of acoustical density perturbations $\rho' \equiv \rho - \rho_0$ at the speed of sound $c_0 = \sqrt{(\partial p/\partial \rho)_S}$ in an homogeneous acoustic medium, emitted by the equivalent source $\partial^2 T_{ij}/\partial x_i \partial x_j$ [1]:

$$\frac{\partial^2 \rho'}{\partial t^2} - c_0^2 \frac{\partial^2 \rho'}{\partial x_i^2} = \frac{\partial^2 T_{ij}}{\partial x_i \partial x_j} \tag{1}$$

where the Lighthill stress tensor $T_{ij} = \rho v_i v_j + (p' - c_0^2 \rho')\boldsymbol{\delta}_{ij} - \sigma_{ij}$ accounts for the sound production by Reynolds stresses, non-isentropic processes and the viscous stresses σ_{ij}.

In this study we consider configurations with large enough Reynolds numbers for the acoustic contribution of the wall-normal dipoles to dominate over the viscous stresses, and we discard the contribution of the latter.

Implementing these assumptions, and assuming a stationary surface, we find

$$\begin{aligned}\rho'(\mathbf{x}, t) = {} & \int_{-\infty}^{t} \iiint_V T_{ij} \frac{\partial^2 G}{\partial y_i \partial y_j} \, \mathrm{d}^3\mathbf{y} \, \mathrm{d}\tau - \int_{-\infty}^{t} \iint_{\partial V} \left\{ c_0^2 \frac{\partial \rho'}{\partial y_i} G + (p' - c_0^2 \rho') \frac{\partial G}{\partial y_i} \right\} n_i \, \mathrm{d}^2\mathbf{y} \, \mathrm{d}\tau \\ & - c_0^2 \int_{-\infty}^{t} \iint_{\partial V} \left(\rho' \frac{\partial G}{\partial y_i} - G \frac{\partial \rho'}{\partial y_i} \right) n_i \, \mathrm{d}^2\mathbf{y} \, \mathrm{d}\tau \end{aligned} \tag{2}$$

The free-field Green's function

$$G(\mathbf{x}, t | \mathbf{y}, \tau) = \frac{\boldsymbol{\delta}(t - \tau - |\mathbf{x} - \mathbf{y}|/c_0)}{4\pi c_0^2 |\mathbf{x} - \mathbf{y}|} \tag{3}$$

is used in (2).

The contribution of the third integral cancels with the density perturbation terms of the second integral in Eq. (2). This yields the classical result:

$$\rho'(\mathbf{x}, t) = \int_{-\infty}^{t} \iiint_V T_{ij} \frac{\partial^2 G}{\partial y_i \partial y_j} \, \mathrm{d}^3\mathbf{y} \, \mathrm{d}\tau - \int_{-\infty}^{t} \iint_{\partial V} p' \frac{\partial G}{\partial y_i} n_i \, \mathrm{d}^2\mathbf{y} \, \mathrm{d}\tau \tag{4}$$

where the presence of the solid boundary appears through the dipole sources distributed over its surface.

Following Batchelor [11], compressibility effects at low-Mach number are due to fast variations related to acoustics. We therefore decompose the pressure field at the wall into two components: a solenoidal part (called hydrodynamic pressure in what follows) and an acoustic component. The hydrodynamic pressure scales with ρU^2 where U is a typical magnitude of the velocity fluctuations in the source region. The energy of the acoustic component scales with the fourth power of the Mach number in proportion to the flow energy. At a wall wetted by low-Mach turbulence, the pressure is thus clearly dominated by near-field hydrodynamic effects. Furthermore, for a compact turbulence–body interaction region, i.e. low Helmholtz numbers $He = kL = 2\pi f D/c_0$, the acoustic contribution to the wall pressure field is irrelevant for the calculation of the dipolar source term of Curle's analogy. An incompressible flow description can then be used to model the acoustic source, as shown by Gloerfelt et al. [6] who successfully predicted the aeolian noise emitted by a cylinder in cross-flow using incompressible CFD data.

In contrast, the prediction of the sound produced by turbulence interacting with non-compact geometries requires the acoustic scattering to be accounted for by the flow model. This, however, is not usually the case for low-Mach numbers, for which incompressible flow modeling is more efficient and therefore preferred. For non-compact cases, the incompressible dipoles must be complemented by an acoustic correction to obtain a realistic sound prediction.

A straightforward correction consists of adopting for Eq. (2) Green's function tailored to the geometry, i.e. having zero normal gradient at the boundary surface. Green's function then accounts for the scattering that is lacking in the flow model. Analytical Green's functions are, however, only known for a limited number of idealized cases, using mirror images of the sources for example in the presence of infinite planes, or calculated by separation of variables when the geometry is aligned with orthogonal directions of a suitable coordinate system. For low frequencies, approximate analytical solutions can be considered, such as Howe's compact Green's functions [12]. In most industrial applications and frequencies of interest, however, the problem is not amenable to an analytical solution, and one must resort to a numerical treatment. For internal problems, building a numerical Green's function based on numerical acoustic modes is possible in theory, but the handling of this function depends on the frequency and on the emitter and listener positions, which is difficult in practice. In Section 3 we propose an original approach, combining Curle's analogy with a BEM, to bring the acoustic correction needed when using incompressible flow data at arbitrary Helmholtz numbers. The results obtained using this approach will be compared to a prediction based on a tailored Green's function, taken as reference solution.

In the remainder of this paper, the inhomogeneous wave propagation equation is considered in the Fourier domain, which takes the form of the Helmholtz equation:

$$\nabla^2 \hat{p}_a + k^2 \hat{p}_a = \hat{q} \tag{5}$$

with $\hat{p}_a e^{i\omega t} = c_0^2 \hat{\rho} e^{i\omega t} = c_0^2 \rho'$, $k = \omega/c_0$, and $\hat{q} = -\partial^2 \hat{T}_{ij}/\partial x_i \partial x_j$ with $T_{ij} = \hat{T}_{ij} e^{i\omega t}$. With some straightforward algebra, Curle's result (4) takes the following form in the Fourier domain:

$$c_0^2 \hat{\rho}(\mathbf{x}, \omega) = \iiint_V \hat{T}_{ij} \frac{\partial^2 \hat{G}}{\partial y_i \partial y_j} \, d^3\mathbf{y} - \iint_{\partial V} \hat{p} \frac{\partial \hat{G}}{\partial y_i} n_i \, d^2\mathbf{y} \tag{6}$$

where the pressure $\hat{p}$ is the full pressure fluctuation (acoustic + hydrodynamic). In Eq. (6), the Fourier domain free-field Green's function is $\hat{G} = \exp(-ikr)/(4\pi r)$. In what follows, the hat notations which indicate Fourier components will be dropped for the sake of readability.

3. Boundary integral formulation of Curle's analogy

The derivation of the boundary integral equation follows the same path as for Curle's analogy. Starting from the Helmholtz equation (5), a convolution with the free-field Green's function G yields

$$c_0^2 \iiint_{V \setminus V_\varepsilon} (\nabla^2 \rho G - \rho \nabla^2 G) \, d^3\mathbf{y} = \iiint_{V \setminus V_\varepsilon} q G \, d^3\mathbf{y} + \iiint_{V \setminus V_\varepsilon} c_0^2 \rho \boldsymbol{\delta}(\mathbf{x} - \mathbf{y}) \, d^3\mathbf{y} \tag{7}$$

There is, however, a significant difference compared to Curle's analogy: an exclusion volume V_ε, which includes the listener's position $\mathbf{x}$, was removed from the integration volume V. This allows Green's theorem to be applied in a domain which is free of the singularity of Green's function kernel at $\mathbf{x} = \mathbf{y}$ [9]. The exclusion volume is usually not necessary in the derivation of Curle's analogy, because the listener is normally placed in the propagation region, defined well away from the source field. Moreover, the numerical resolution of the boundary integral equation is performed by collocation, i.e. by placing the listener directly on the source surface. This singularity is excluded by removing the volume V_ε from the source integration, so that the contribution of the third integral of Eq. (7) is equal to zero.

Applying Green's theorem to the LHS of Eq. (7), we find

$$Cc_0^2\rho = c_0^2 \iint_{\partial V} \left(\frac{\partial \rho}{\partial n} G - \rho \frac{\partial G}{\partial n} \right) \mathrm{d}^2\mathbf{y} + \lim_{\varepsilon \to 0} \iiint_{V \backslash V_\varepsilon} \frac{\partial^2 T_{ij}}{\partial y_i \partial y_j} G \, \mathrm{d}^3\mathbf{y} \tag{8}$$

where the factor C is the solid angle seen by the point $\mathbf{x}$ in the exclusion volume V_ε. It is equal to 1 when the $\mathbf{x}$ is within the volume, and equal to $\frac{1}{2}$ when $\mathbf{x}$ lies over a smooth surface of the body. Integrating the last integral by parts, and evaluating the limit for the scattering integral as before, yields

$$Cc_0^2\rho = \iiint_V T_{ij} \frac{\partial^2 G}{\partial y_i \partial y_j} \mathrm{d}^3\mathbf{y} + \iint_{\partial V} \left(-c_0^2 \frac{\partial \rho}{\partial n} G - (p - c_0^2 \rho) \frac{\partial G}{\partial n} \right) - C(p - c_0^2 \rho) + c_0^2 \iint_{\partial V} \left(\frac{\partial \rho}{\partial n} G - \rho \frac{\partial G}{\partial n} \right) \mathrm{d}^2\mathbf{y} \tag{9}$$

This can be simplified as

$$Cp = \iiint_V T_{ij} \frac{\partial^2 G}{\partial y_i \partial y_j} \mathrm{d}^3\mathbf{y} - \iint_{\partial V} p \frac{\partial G}{\partial n} \mathrm{d}^2\mathbf{y} \tag{10}$$

which is fairly similar to the result derived in the classical analogy of Curle (4), except for differences related to the change from the time to the frequency domain, including the factor c_0^2 due to the different Green's functions in the time and frequency domains. It should, however, be noted that Eq. (10) yields the full pressure fluctuations, while Eq. (4) is usually employed to obtain the acoustic component only. This results from having let the listener enter the source region, while in Curle's analogy the listener is often assumed to be in a uniform and quiescent propagation region well apart from the sound production region. As a corollary, form (10) can be seen as an implicit integral equation giving the pressure at any point in the flow field, including at the body surface, provided the volumetric term is known. The result of Curle's analogy is readily recovered when placing the listener in a quiescent medium, as the LHS of Eq. (10) can only account for acoustic perturbations there.

Without loss of generality, we let the pressure fluctuation be expressed as the sum of a hydrodynamic and an acoustic component: $p = p_\mathrm{h} + p_\mathrm{a}$. The hydrodynamic pressure fluctuation satisfies the Poisson equation

$$\nabla^2 p_\mathrm{h} = -\frac{\partial \rho_0 v_i v_j}{\partial x_i \partial x_j} \tag{11}$$

We then decompose the integration domain of Eq. (10) into two parts, which correspond, respectively, to volumes V_1 and V_2, and their boundaries ∂V_1 and ∂V_2, as indicated in Fig. 1:

$$C(p_\mathrm{h} + p_\mathrm{a}) = \iiint_{V_1} T_{ij} \frac{\partial^2 G}{\partial y_i \partial y_j} \mathrm{d}^3\mathbf{y} - \iint_{\partial V_1} (p_\mathrm{h} + p_\mathrm{a}) \frac{\partial G}{\partial n} \mathrm{d}^2\mathbf{y} + \iiint_{V_2} T_{ij} \frac{\partial^2 G}{\partial y_i \partial y_j} \mathrm{d}^3\mathbf{y} - \iint_{\partial V_2} (p_\mathrm{h} + p_\mathrm{a}) \frac{\partial G}{\partial n} \mathrm{d}^2\mathbf{y} \tag{12}$$

The domain V_1 is localized around the collocation point $\mathbf{x}$, and is acoustically compact. The domain V_2 is defined as $V \backslash V_1$. An integral solution for the Poisson equation (11) can be derived on the compact volume V_1

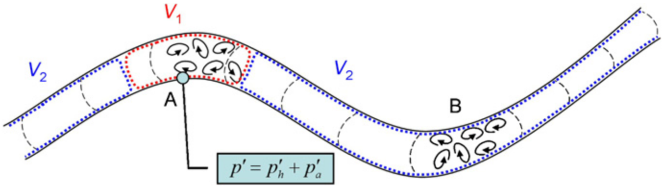

Fig. 1. At the collocation node, we decompose the wall pressure into a near-field hydrodynamic component due to the scattering of turbulence in V_1, and an acoustic component radiated by remote turbulence in V_2.

to yield

$$Cp_{\mathrm{h}} = \iiint_{V_1} \rho_0 v_i v_j \frac{\partial^2 G}{\partial y_i \partial y_j} \,\mathrm{d}^3\mathbf{y} - \iint_{\partial V_1} p_{\mathrm{h}} \frac{\partial G}{\partial n} \,\mathrm{d}^2\mathbf{y} \tag{13}$$

For low-Mach numbers, the Lighthill tensor in Eq. (12) can be approximated by $T_{ij} \approx \rho_0 v_i v_j$, and subtracting Eq. (13) from Eq. (12) yields

$$\begin{aligned} Cp_{\mathrm{a}} &= -\iint_{\partial V_1} p_{\mathrm{a}} \frac{\partial G}{\partial n} \,\mathrm{d}^2\mathbf{y} + \iiint_{V_2} \rho_0 v_i v_j \frac{\partial^2 G}{\partial y_i \partial y_j} \,\mathrm{d}^3\mathbf{y} - \iint_{\partial V_2} (p_{\mathrm{h}} + p_{\mathrm{a}}) \frac{\partial G}{\partial n} \,\mathrm{d}^2\mathbf{y} \\ &= -\iint_{\partial V} p_{\mathrm{a}} \frac{\partial G}{\partial n} \,\mathrm{d}^2\mathbf{y} + \iiint_{V_2} \rho_0 v_i v_j \frac{\partial^2 G}{\partial y_i \partial y_j} \,\mathrm{d}^3\mathbf{y} - \iint_{\partial V_2} p_{\mathrm{h}} \frac{\partial G}{\partial n} \,\mathrm{d}^2\mathbf{y} \end{aligned} \tag{14}$$

where the boundary integrals involving the acoustic pressure p_{a} have been grouped together.

To summarize, the wall pressure can be expressed as the sum of a hydrodynamic component, which can be obtained by an incompressible flow model, and an acoustic component, which is the solution of Eq. (14). This integral implicit equation can be classically resolved using a BEM, considering the two last integrals as an incident field. Once the acoustic component of the wall pressure field has been obtained, it must be summed with the hydrodynamic component to yield the complete dipole source term of Curle's analogy. The classic formulation (4) is then used to obtain the acoustic field at the listener's position in the propagation region.

The boundary integral formulation (14) is resolved by approximating the continuous distribution of the variables by a prescribed functional form defined over small elements [9]:

$$p(\mathbf{y}) = \sum_{j=1}^{n_e} N_j^e(\mathbf{y}) p_j \tag{15}$$

where p_j is the value taken by the pressure field at the node j of the element e. Each shape function N_j^e is locally defined such that it has a unit value at the node j of the element e, and is equal to zero at all the other nodes of that element. Global shape functions are defined over the whole domain, equal to the element shape functions for elements connected to the node j and equal to zero elsewhere, to yield global variable expansions, in matrix form

$$p(\mathbf{y}) = [N_j]\{p_j\} \tag{16}$$

where $[N_j]$ is a $(1 \times n_{\mathrm{a}})$ vector of global shape functions and $\{p_j\}$ is an $(n_{\mathrm{a}} \times 1)$ vector of unknown pressures. Inserting this boundary element approximation in Eq. (14), one obtains

$$Cp_{\mathrm{a}} = -\{p_{\mathrm{a}j}\} \iint_{\partial V} [N] \frac{\partial G}{\partial n} \,\mathrm{d}^2\mathbf{y} - \{p_{\mathrm{h}k}\} \iint_{\partial V_2} [N] \frac{\partial G}{\partial n} \,\mathrm{d}^2\mathbf{y} + Q \tag{17}$$

where Q represents the volume integral of Lighthill's tensor. Eq. (17) is resolved by collocation, placing the listener at the acoustic nodes $\mathbf{x}_i$, $i = 1 \dots n_{\mathrm{a}}$:

$$C_i p_{\mathrm{a}i} = -[A'_{ij}]\{p_{\mathrm{a}j}\} - [A''_{ik}]\{p_{\mathrm{h}k}\} \tag{18}$$

where the matrices

$$\begin{aligned} [A'_{ij}] &= \iint_{\partial V} [N_j] \frac{\partial G(\mathbf{x}_i, \mathbf{y}_j)}{\partial n} \,\mathrm{d}^2\mathbf{y} \\ [A''_{ik}] &= \iint_{\partial V_2} [N_k] \frac{\partial G(\mathbf{x}_i, \mathbf{y}_k)}{\partial n} \,\mathrm{d}^2\mathbf{y} \end{aligned}$$

merely differ by the extent of the integration volume. The first integral is performed over all boundary elements $j = 1 \dots n_{\mathrm{a}}$ of the acoustic domain, while the second integral concerns only the elements $k = 1 \dots n_{\mathrm{h}}$ wetted by turbulence that are part of ∂V_2, i.e. that are situated beyond the hydrodynamic field of the point i. The domain V_2 is therefore dependent on the location of the node i. A more convenient form is obtained by expressing Eq. (18) as

$$C_i p_{\mathrm{a}i} = -[A'_{ij}]\{p_{\mathrm{a}j}\} - [A'_{ij}][W_{jk}]\{p_{\mathrm{h}k}\} \tag{19}$$

where expression (18) is obtained by having the elements of the weighting matrix $[W_{jk}]$ equal to 0 when the element j is part of ∂V_1, and equal to 1 when this element is part of ∂V_2. Form (19) is advantageous because it does not require the additional calculation of the matrix $[A''_{ij}]$, the matrix $[A'_{ij}]$ being calculated in any case, and because it allows a transition function between the hydrodynamic and acoustic fields around the node i to be modeled explicitly.

4. Validation of the approach

The validation benchmark is a two-dimensional case of two filament vortices spinning within an infinite duct. This test case was previously introduced by the present authors to demonstrate the inadequacy of Curle's analogy for non-compact flows in ducts [7]. The simplicity of this configuration allows an analytical derivation of the flow and acoustic fields, therefore permitting validation of the proposed numerical technique. Moreover, it exhibits the main difficulty addressed in this paper: wall–turbulence interaction over a non-compact source region.

The sound prediction is obtained in two ways. The first approach consists of using a tailored Green's function, built from the duct modes [3]. This approach provides the reference solution, which does not involve the pressure information at the duct walls where the wall-normal gradient of Green's function is zero. The second method is our BEM/Curle formulation, using a free-field Green's function and involving the contribution of the perturbation pressure at the walls in addition to the volumetric source term.

4.1. Flow model

An incompressible flow description is obtained by integrating the reciprocal Biot–Savart induction of the two spinning vortices. The two-dimensional velocity field (u, v) is derived from the complex velocity potential: $u - \mathrm{i}v = \mathrm{d}w/\mathrm{d}z$, where $z = x + \mathrm{i}y$ is the complex coordinate, in a coordinate system having the x-axis aligned with the duct symmetry axis.

For a vortex filament placed within an infinite straight duct of height h, an infinite network of image vortices must be added to satisfy the non-penetration velocity boundary condition at the upper and lower walls, as

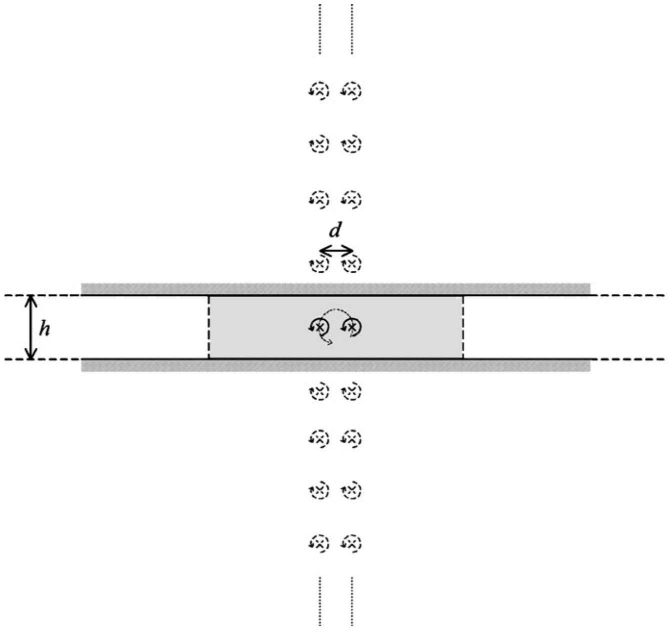

Fig. 2. Two rectilinear filament vortices within an infinite two-dimensional straight duct.

shown in Fig. 2. The resulting velocity potential due to the vortex n at the coordinate z_n is therefore

$$w(z) = -\frac{\mathrm{i}\Gamma}{2\pi}\{\log(z - z_n) - \log[z - (z_n + \mathrm{i}h - 2\mathrm{i}y_1)] + \log[z - (z_n - 2\mathrm{i}h)] - \cdots - \log[z - (z_n - \mathrm{i}h - 2\mathrm{i}y_1)] + \log[z - (z_n + 2\mathrm{i}h)] + \cdots\} \tag{20}$$

where Γ, the circulation of each vortex, has been adjusted such that significant harmonics of the corresponding acoustic source terms excite transverse modes of the duct (in the y-direction). The free parameters are $\Gamma = 85\,\mathrm{m}^2\,\mathrm{s}^{-1}$, the duct height $h = 1\,\mathrm{m}$ and the density $\rho = 1.225\,\mathrm{kg\,m}^{-3}$, which are used to normalize the other quantities. The vortex filaments are initially placed over the duct axis, separated by a distance $d = h/2$. The relevant velocity and Mach numbers are $U = \Gamma/d$ and $M = \Gamma/(dc_0) = 0.5$ with a speed of sound $c_0 = 340\,\mathrm{m\,s}^{-1}$. For such Mach numbers, the application of an incompressible flow model can be questionable. However, the error scales with the square of the Mach number [13], and furthermore our results discussed in Section 4.3 indicate that this approximation does not compromise the validation.

The calculation of the velocity field inside the duct and of the wall pressure field, induced by the two spinning vortex filaments shown in Fig. 2, is performed in two steps. In the first step, the trajectories of the two vortices are integrated in time, by evaluating the velocity field induced at each vortex position by the other filament. The velocity field over the whole duct domain can then be obtained from the complex potential induced by the two vortices at each time step.

The ODE45 function of Matlab 6.5 was used to solve the trajectories of the two vortices by time-marching the equations for the position of each vortex filament m, induced by its own potential and the potential due to the other vortex n, accounting for their images:

$$u_m = -\frac{\Gamma}{4h}\left\{\frac{\sin[\pi(y_m - y_n)/h]}{\cosh[\pi(x_m - x_n)/h] - \cos[\pi(y_m - y_n)/h]} + \frac{\sin[\pi(y_m + y_n)/h]}{\cosh[\pi(x_m - x_n)/h] + \cos[\pi(y_m + y_n)/h]} + \frac{\sin(2\pi y_m/h)}{1 + \cos(2\pi y_m/h)}\right\} \tag{21}$$

$$v_m = -\frac{\Gamma}{4h}\left\{\frac{-\sinh[\pi(x_m - x_n)/h]}{\cosh[\pi(x_m - x_n)/h] - \cos[\pi(y_m - y_n)/h]} + \frac{\sinh[\pi(x_m - x_n)/h]}{\cosh[\pi(x_m - x_n)/h] + \cos[\pi(y_m + y_n)/h]}\right\} \tag{22}$$

for $m, n = 1, 2$ $(m \neq n)$.

Integrating the unsteady Bernoulli equation

$$\frac{\partial \Phi}{\partial t} + \frac{|\mathbf{v}|^2}{2} + \int \frac{\mathrm{d}p}{\rho} = 0 \tag{23}$$

along each wall—forming a streamline in this inviscid problem, yields the unsteady pressure distribution at the walls:

$$\rho\frac{\partial \Phi_w}{\partial t} + \rho\frac{|\mathbf{v}_w|^2}{2} + p_w = \rho\frac{\partial \Phi_\infty}{\partial t} + \rho\frac{|\mathbf{v}_\infty|^2}{2} + p_\infty \tag{24}$$

where the right-hand side vanishes at infinity by choosing a zero reference pressure at infinity. The wall pressure is related to the local values of the velocity potential and slip velocity:

$$p_w = -\rho\left(\frac{\partial \Phi_w}{\partial t} + \frac{u_w^2}{2}\right) \tag{25}$$

Once the kinematics of the vortices have been integrated, the velocity field at any point within the duct, except at the filament positions, can be obtained from the summed velocity potentials of the two vortices (20) with $n = 1, 2$. However, a different approach was required in order to avoid the singularity of the velocity field at the locations of the vortex filaments. At every time step, velocity fields corresponding to Oseen velocity distributions

$$v_\theta(r) = \frac{\Gamma}{2\pi r}\left[1 - \exp\left(-\frac{r^2}{2\sigma^2}\right)\right] \tag{26}$$

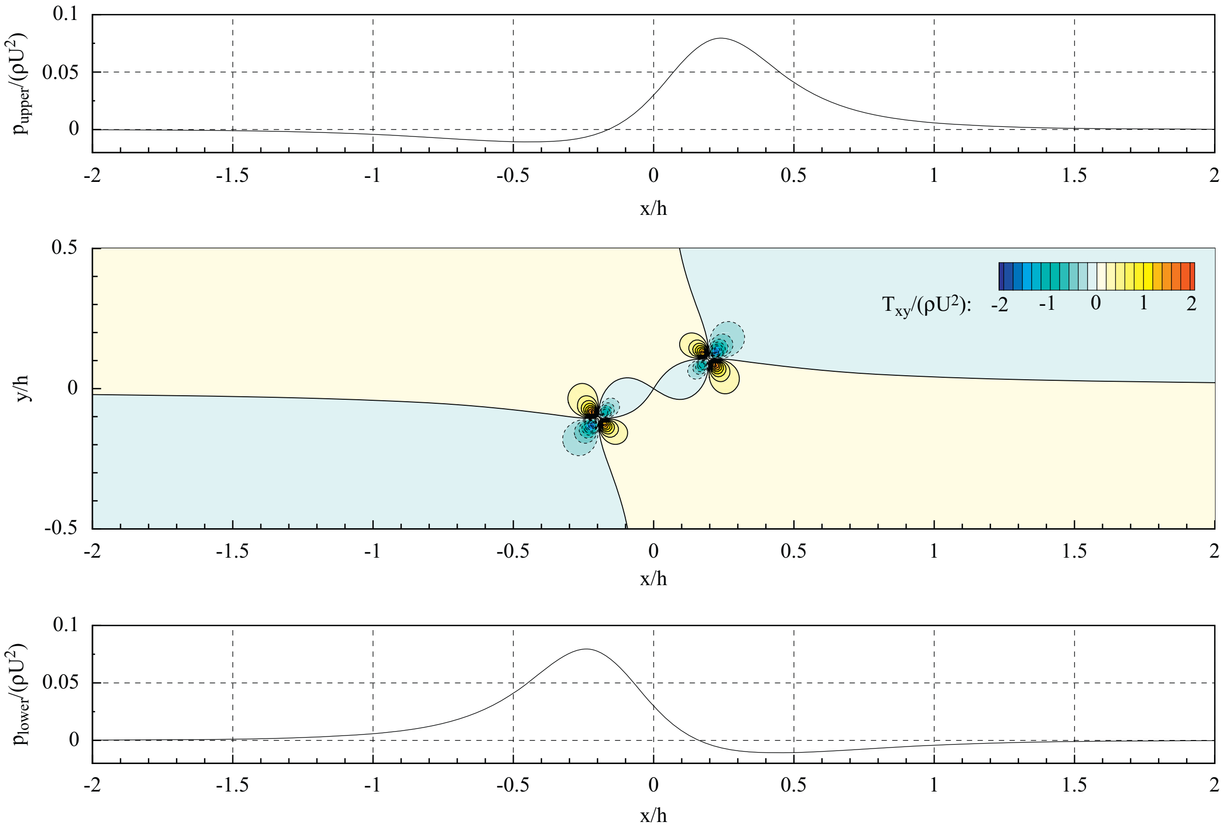

Fig. 3. Acoustic source region: instantaneous Lighthill's tensor $T_{xy} = \rho_0 uv$ and instantaneous pressure over both upper and lower walls.

with core sizes σ were generated for each vortex position and summed together. Fig. 3 illustrates, for a single time step, the component $T_{xy} = \rho_0 uv$ of Lighthill's tensor and of the wall pressure over the region considered for the integration of the source field ($x/h \in [-2, 2]$). It can be verified that this domain includes significant quadrupole and dipole sources.

Fig. 4 displays the Fourier transform of the Lighthill tensor T_{xy} at the position $(x/h, y/h) = (0.25, 0)$, where a significant number of harmonics of the main rotation frequency are seen. These harmonics are due to the modulation of the velocities of the vortices caused by the presence of their image vortices. It was observed that the higher harmonic content increases with the initial spacing between the two vortex filaments due to the enhanced influence of the image vortices, though at harmonics of a lower fundamental frequency.

The core sizes σ are kept small compared to the distance between the vortices to be consistent with the filament-based mutual induction model described above. This constitutes at this stage the only approximation in the derivation of the flow model. Sensitivity analyses have been carried out to investigate the impact of the desingularized core size on the sound production, the results of which are detailed in Appendix B.

4.2. Two-dimensional tailored Green's function

The duct tailored Green's function, solution of the two-dimensional Helmholtz equation

$$\nabla_2^2 G_1 + k^2 G_1 = \boldsymbol{\delta}(x - x_0)\boldsymbol{\delta}(y - y_0) \quad \text{with } k = \omega/c_0 \tag{27}$$

with Neumann boundary conditions $\partial G/\partial n = 0$ at the walls, is found by separation of variables: $G_1 = \sum_n F_n(x)\Psi_n(y)$, with $F_n(x) = A_n \mathrm{e}^{\mp \mathrm{i} k_n (x - x_0)}$ and $\Psi_n(y) = \cos(n\pi y/h)$. The amplitude A_n of each mode is found by imposing continuity of the solution at the source position. We find the two-dimensional tailored

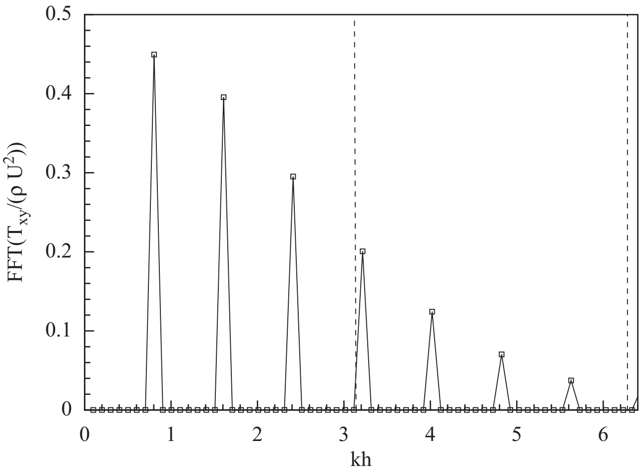

Fig. 4. Fourier transform of the Lighthill's tensor T_{xy} at the coordinate $(x/h, y/h) = (0.25, 0)$.

Green's function:

$$G_1 = \frac{\mathrm{i}}{2h}\sum_{n=0}^{\infty}\frac{1}{C_n k_n}\cos(\eta_n y_0)\cos(\eta_n y)\mathrm{e}^{\mp \mathrm{i}k_n(x-x_0)} \tag{28}$$

where $k_n = n\omega/c_0$, $\eta_n = n\pi/h$, and

$$C_n = \begin{cases} 1 & \text{if } n = 0 \\ 1/2 & \text{if } n \neq 0 \end{cases} \tag{29}$$

Note that expression (28) corresponds to a coordinate system having its x-axis aligned with the lower wall. Substituting the tailored Green's function (28) into Eq. (6) rewritten for a two-dimensional problem yields the expansion for the acoustic pressure:

$$\begin{aligned} p_\mathrm{a}(\mathbf{x},\omega) = &-\frac{\mathrm{i}}{2h}\sum_{n=0}^{\infty}\frac{\cos(\eta_n y)}{k_n C_n}\left\{k_n^2\iint_{S_0}\cos(\eta_n y_0)\rho_0 u^2 \mathrm{e}^{\mp \mathrm{i}k_n(x-x_0)}\,\mathrm{d}x_0\,\mathrm{d}y_0 + \eta_n^2\iint_{S_0}\cos(\eta_n y_0)\rho_0 v^2 \mathrm{e}^{\mp \mathrm{i}k_n(x-x_0)}\,\mathrm{d}x_0\,\mathrm{d}y_0\right. \\ &\left.\pm\, \mathrm{i}k_n\eta_n\iint_{S_0}\sin(\eta_n y_0)\rho_0 uv\mathrm{e}^{\mp \mathrm{i}k_n(x-x_0)}\,\mathrm{d}x_0\,\mathrm{d}y_0\right\} \end{aligned} \tag{30}$$

where S_0 is the domain between $x/h = -2$ and 2, large enough to include significant sources as shown in Fig. 3. The series is truncated beyond a sufficient number of evanescent modes to converge in the mid- to far field. Apart from this truncation, Eq. (30) is an exact solution of the ducted vortex spinning problem.

4.3. Application of the BEM/Curle formulation

The BEM formulation (19) has been implemented in the commercial code SYSNOISE Rev 5.6. Because this solver is mainly developed for three-dimensional problems, while our reference solution based on the tailored Green's function is valid in two dimensions x and y, the three-dimensional calculations were performed using a BEM mesh with a thickness in the z-direction small enough for transverse modes in that direction to be cut-off for the frequency range of interest (Fig. 5). A straightforward comparison with the two-dimensional results is then performed through a scaling of the three-dimensional BEM results by the duct thickness. The duct extends in the axial direction between $x/h = -5$ and 5, has a unit height, and extends in the z-direction from $z/h = -0.1$ to 0.1. The cut-off frequency in the z-direction is thus equal to $kh = 15.71$, well above the frequencies considered here.

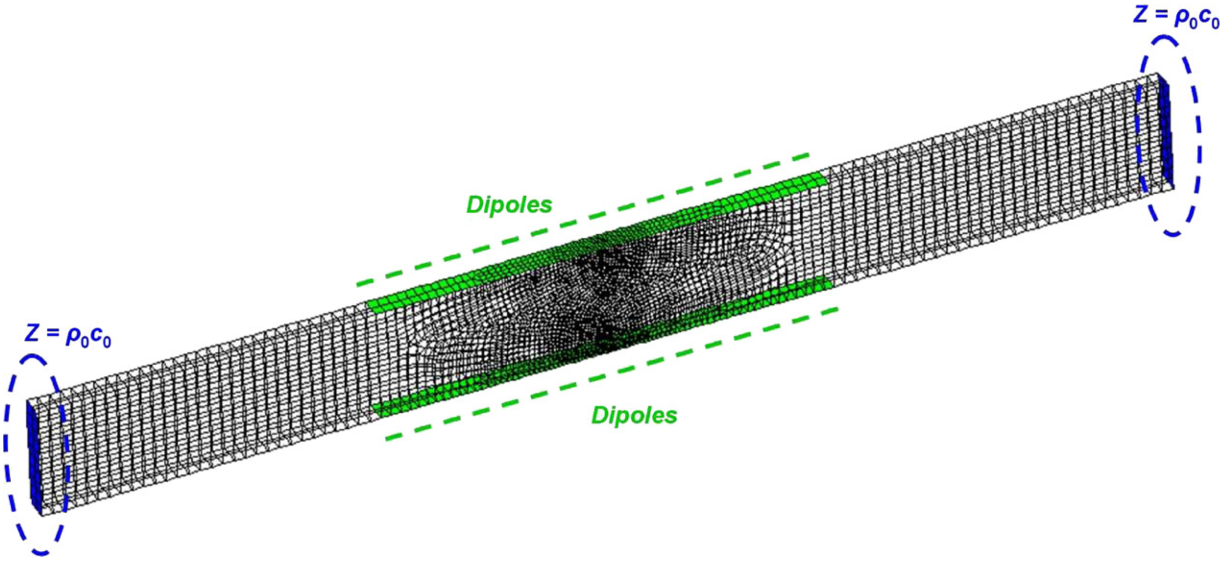

Fig. 5. BEM model mesh used to compute the sound emitted by the two spinning vortices. Anechoic boundary conditions are applied to the duct ends, and dipole boundary conditions are applied to the duct upper and lower walls in the source region.

4.4. *Sampling and integration of the dipoles and quadrupoles*

The quadrupole and dipole sources have been introduced in the BEM acoustic model after pre-processing in Matlab 6.5. The two-dimensional quadrupoles obtained from the vortex model have been Fourier-transformed and integrated in the z-direction, and in the (x, y) plane over cells with dimension $0.05h$ in both directions. The dipoles are generated by mapping the Fourier-transformed unsteady pressure over the upper and lower duct walls.

4.5. *Non-reflecting boundary conditions*

Non-reflecting boundary conditions are applied at both ends of the duct, in order to permit comparison with the infinite duct reference solution. This was achieved by setting an acoustical impedance $Z = \rho_0 c_0$ at both ends of the duct model mesh. This boundary condition is exactly anechoic for plane wave propagation, but is not so for higher modes. We investigated this aspect by placing a monopole source in our duct, at the coordinate $(x/h, y/h, z/h) = (0, 0.35, 0)$, and propagating it in the duct with $Z = \rho_0 c_0$ boundary conditions at both duct ends. The acoustic pressure was solved for frequencies covering the range $kh = [1 \ldots 8]$, and compared with the exact solution obtained using the tailored Green's function for an infinite duct (28). Fig. 6 shows the acoustic pressure at the coordinate $(x/h, y/h, z/h) = (2, 0.65, 0)$ obtained by the BEM solver with $Z = \rho_0 c_0$ boundary conditions (dashed line) and the exact solution (continuous line). It shows that the numerical solution follows the analytical solution up to the cut-off frequency ($kh = \pi$), just above which some wiggles somewhat deteriorate the numerical prediction. The agreement becomes fair again for increasing frequencies, until the second transverse mode ($kh = 2\pi$), the deviations being substantially higher above that limit. It can be concluded from these numerical tests that a prediction of the BEM prediction with the exact reference solution for infinite duct is not only meaningful below the cut-off frequency, but also for some frequencies within the interval between the first and second cut-off.

4.6. *Sound emitted by the ducted vortex pair spinning*

The exact solution (30) and our combined BEM/Curle approach (19) are finally compared.

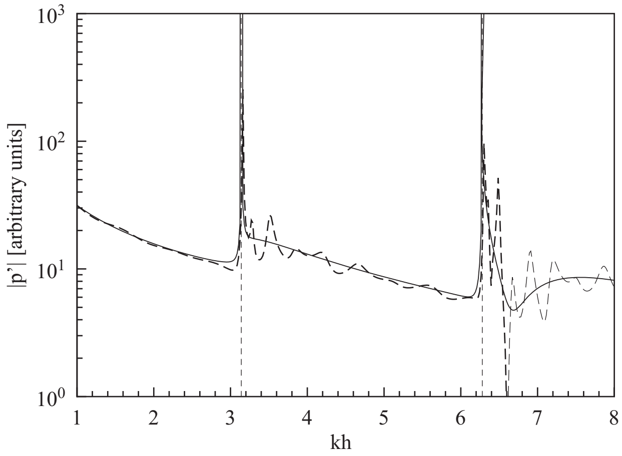

Fig. 6. Acoustic response of the duct shown in Fig. 5, for a unit monopole at the position $(x/h, y/h) = (0, 0.35)$, evaluated at a listener positioned at $(x/h, y/h) = (2, 0.65)$. —, exact solution based on tailored Green's function; − − −, BEM solution with $Z = \rho_0 c_0$ boundary conditions.

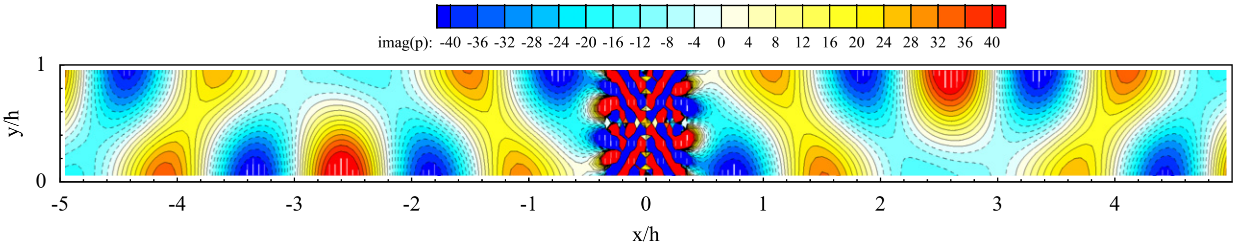

Fig. 7. Sound pressure field (imaginary part) produced by the ducted spinning, $kh = 4.8$. Using tailored Green's function (reference solution).

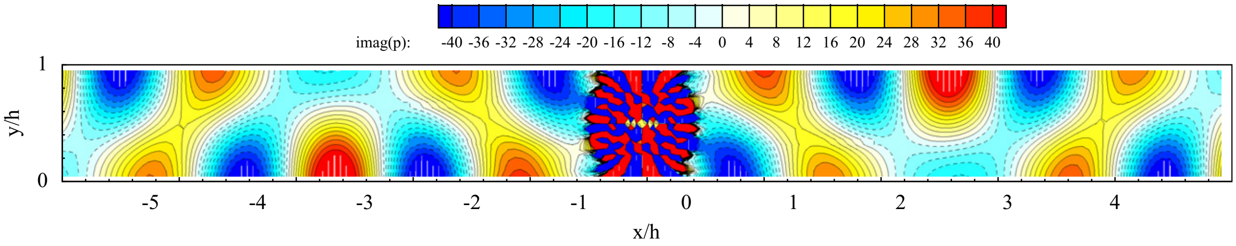

Fig. 8. Sound pressure field (imaginary part) produced by the ducted spinning, $kh = 4.8$. Dipoles and quadrupoles using new formulation (14).

Figs. 7 and 12 show the reference solution obtained using the tailored Green's function. Figs. 8 and 13 show the numerical solution obtained by applying our BEM/Curle approach. While it was shown by Schram [7] that a straightforward application of Curle's classical analogy can yield erroneous results for this benchmark, it is now demonstrated that the BEM/Curle method yields excellent agreement with the reference data. A few discrepancies are found in the near field of the source region, which can be attributed to the poor convergence of the tailored Green's function, based on trigonometric functions, to represent the acoustic near-field.

Figs. 9 and 14 show the dipole contribution to the total field of Figs. 8 and 13, i.e. obtained by applying Eq. (14) without the quadrupole incident field. Similarly, Figs. 10 and 15 show the contribution of the

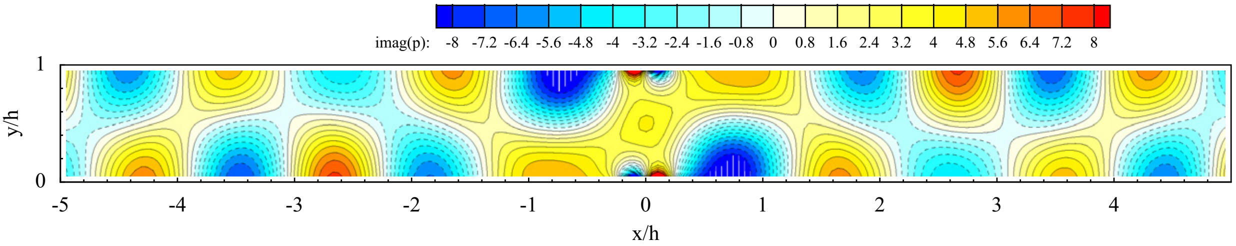

Fig. 9. Sound pressure field (imaginary part) produced by the ducted spinning, $kh = 4.8$. Dipolar contribution alone.

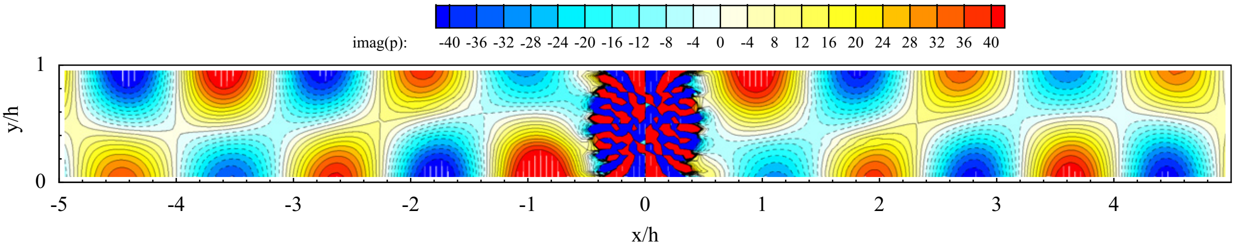

Fig. 10. Sound pressure field (imaginary part) produced by the ducted spinning, $kh = 4.8$. Quadrupolar contribution T_{ij} alone.

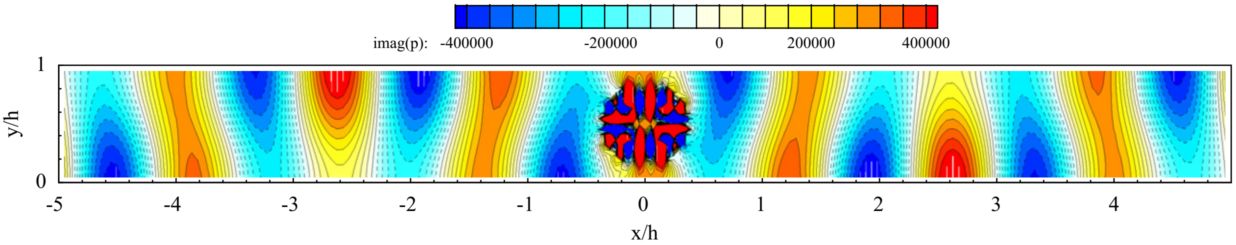

Fig. 11. Sound pressure field (imaginary part) produced by the ducted spinning, $kh = 4.8$. Using monopole sources $\partial^2 T_{ij}/\partial y_i \partial y_j$.

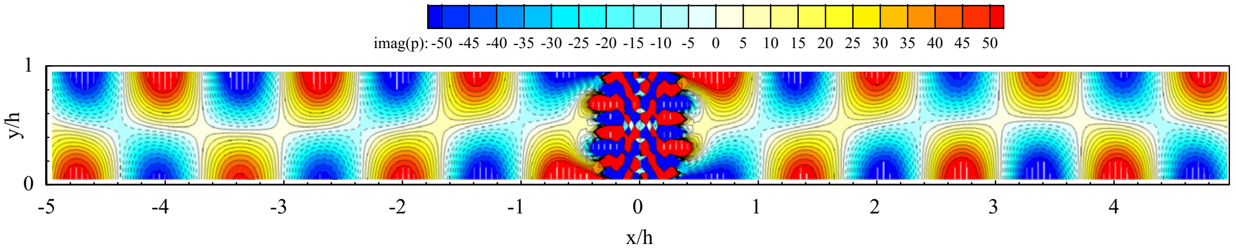

Fig. 12. Sound pressure field (imaginary part) produced by the ducted spinning, $kh = 5.6$. Using tailored Green's function (reference solution).

quadrupoles $\rho_0 uv$ only. We observe that the dipoles contribute to approximately only $\frac{1}{5}$th of the total field, though the quadrupole field alone does not suffice to obtain the correct pressure pattern. The importance of the quadrupole contribution is related to the relatively high-Mach number, making the source region substantially non-compact. Moreover, in this straight duct case the dipoles merely represent the mirrored reflections of the quadrupoles, and have thus at most a similar acoustic efficiency.

Finally, Figs. 11 and 16 show the acoustic field obtained by scattering the source of Lighthill's equation (1), i.e. the double divergence of Lighthill's tensor herein approximated as $\partial^2 \rho_0 uv/\partial x \partial y$ and accordingly regarded as a monopole. This result displays an acoustic field having an error four orders of magnitude larger than the

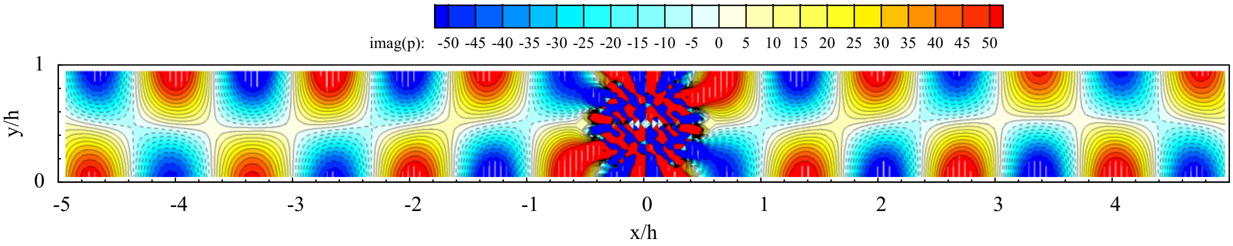

Fig. 13. Sound pressure field (imaginary part) produced by the ducted spinning, $kh = 5.6$. Dipoles and quadrupoles using new formulation (14).

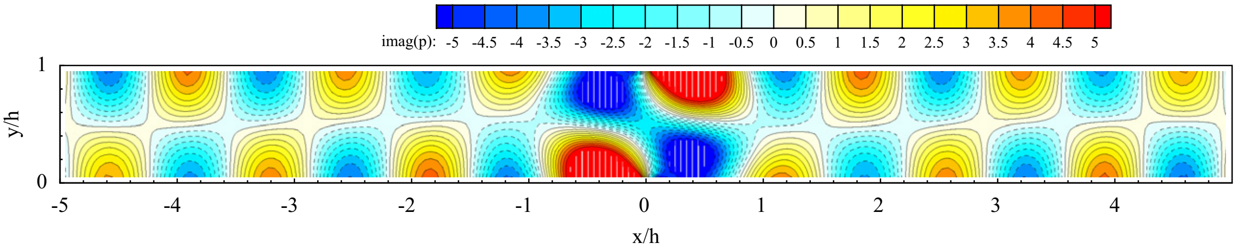

Fig. 14. Sound pressure field (imaginary part) produced by the ducted spinning, $kh = 5.6$. Dipolar contribution alone.

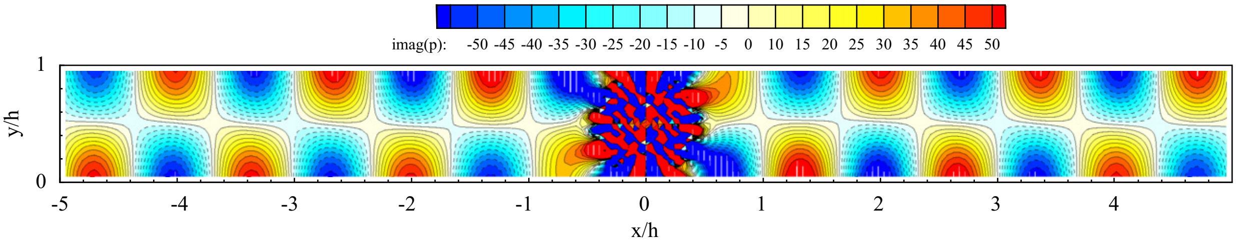

Fig. 15. Sound pressure field (imaginary part) produced by the ducted spinning, $kh = 5.6$. Quadrupolar contribution T_{ij} alone.

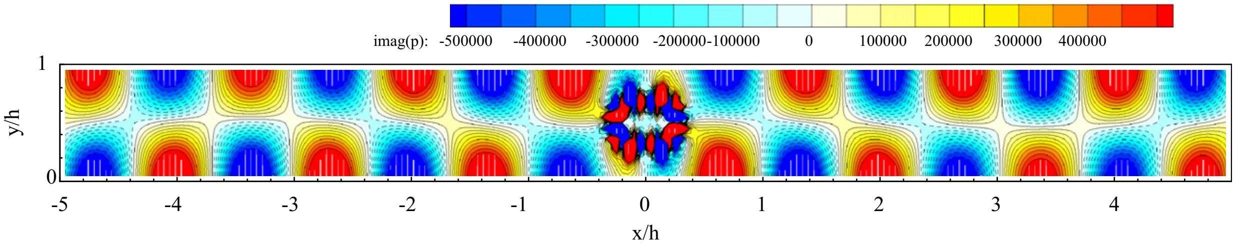

Fig. 16. Sound pressure field (imaginary part) produced by the ducted spinning, $kh = 5.6$. Using monopole sources $\partial^2 T_{ij}/\partial y_i \partial y_j$.

reference simulation. This highlights a known fact: the dramatic fragility of the acoustic analogy when the correct multipole order is not imposed by the formulation. Though exact from a formal viewpoint, Eq. (1) expresses the source as a distribution of monopoles, with the result that numerical errors behave as monopoles as well and are therefore much more efficient radiators than the desired quadrupole field. These errors are known to remain as leading order once all the source cancelations have been accounted for.

Results at other frequencies are displayed in Fig. 17, with harmonics 3–7 of the source displayed in Fig. 4. The agreement is excellent for all frequencies except the fourth harmonics at $kh = 3.2$, where there are some

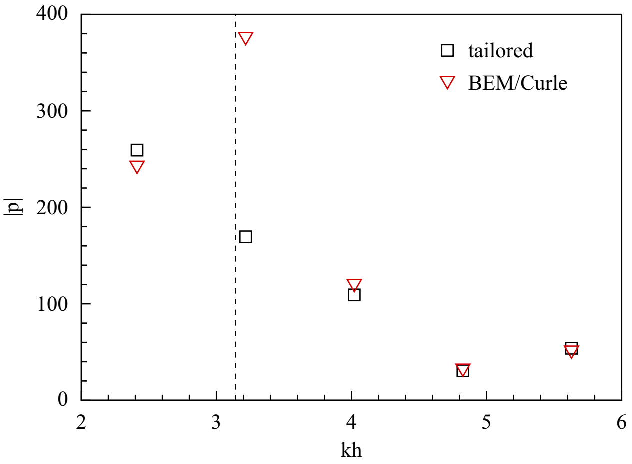

Fig. 17. Sound pressure field (amplitude) obtained by our BEM/Curle approach (19), compared to the exact solution (30).

discrepancies. This is due to the inappropriate boundary condition $Z = \rho_0 c_0$ whose effect was shown in Fig. 19 to be most noticeable just above the cut-off frequencies of the duct.

5. Conclusions

An innovative approach, combining the BEM with Curle's analogy, is proposed in this work. It has been applied to an interesting inviscid and incompressible flow model for computational aeroacoustics: the sound produced by two spinning vortex filaments in an infinite two-dimensional duct. Both the flow and acoustic fields can be addressed analytically, with a low level of approximation. The results demonstrate excellent agreement between the numerical and theoretical acoustic fields, at all frequencies for which an approximate anechoic boundary condition was shown to be suitable.

While Curle's analogy has been mostly applied to compact geometries, the proposed hybrid method permits solving the acoustic propagation in geometries of arbitrary extent and complexity, still taking advantage of the computational efficiency of Curle's analogy at low-Mach numbers. This approach allows an incompressible model of the flow field to be used, which is a significant advantage considering that compressible flow solvers face stiffness issues and converge only slowly to a workable flow solution at low-Mach numbers.

Acknowledgments

The authors are grateful to the Flemish Institute for scientific and technological innovation in industry (IWT) for their support, provided in the framework of the project CAPRICORN (contract SBO 050163).

Appendix A. Velocity field and wall pressure field induced by two filament vortices in an infinite two-dimensional duct

The two-dimensional velocity field (u, v) is derived from the complex velocity potential: $u - \mathrm{i}v = \mathrm{d}w/\mathrm{d}z$, where $z = x + \mathrm{i}y$ is the complex coordinate. The calculation of the velocity field inside the duct and of the wall pressure field, induced by the two spinning vortex filaments shown in Fig. 2, is performed in two steps. In the first step, the trajectories of the two vortices are integrated in time, by evaluating the velocity field at each vortex position. The velocity field over the whole duct domain is then obtained from the complex potential induced by the two vortices at each time step.

The two-dimensional, complex velocity potential of a straight vortex filament is $w(z) = \Phi + \mathrm{i}\Psi = (-\mathrm{i}\Gamma/2\pi)\log(z - z_1)$, where Φ is the real velocity potential, Ψ is the stream function, z_1 is the position of the vortex and Γ is the vortex circulation.

For a vortex filament placed within an infinite straight duct of height h, an infinite network of image vortices must be added to satisfy the non-penetration velocity boundary condition at the upper and lower walls, respectively, located at the coordinates $z = \mathrm{i}h/2$ and $-\mathrm{i}h/2$ according to the coordinate system shown in Fig. 2. The resulting velocity potential due to the vortex n at the coordinate z_n is therefore

$$\begin{aligned} w(z) = & -\frac{\mathrm{i}\Gamma}{2\pi}\{\log(z - z_n) \\ & - \log[z - (z_n + \mathrm{i}h - 2\mathrm{i}y_n)] + \log[z - (z_n - 2\mathrm{i}h)] - \cdots \\ & - \log[z - (z_n - \mathrm{i}h - 2\mathrm{i}y_n)] + \log[z - (z_n + 2\mathrm{i}h)] + \cdots\} \end{aligned} \tag{A.1}$$

where

- the first line corresponds to the vortex filament within the duct,
- the second line sums the contributions of the vortex images due to the upper wall (including the image of this image by the lower wall, and so on),
- the third line sums the contributions of the image of the vortex due to the lower wall (including the image of this image due to the upper wall, and so on).

The two infinite sums of velocity potentials can be expressed as a series, to yield the potential at the point m, due to the vortex n:

$$\begin{aligned} w_n(z) = & -\frac{\mathrm{i}\Gamma}{2\pi}\log\left\{\frac{(z - z_n)\prod_{k=1}^{\infty}[(z - z_n)^2 + 4k^2h^2]}{\prod_{k=1}^{\infty}[(z - \tilde{z}_n)^2 + (2k-1)^2h^2]}\right\} \\ = & -\frac{\mathrm{i}\Gamma}{2\pi}\log\left\{C\frac{(z - z_n)\prod_{k=1}^{\infty}[1 + (z - z_n)^2/(4k^2h^2)]}{\prod_{k=1}^{\infty}[1 + (z - \tilde{z}_n)^2/((2k-1)^2h^2)]}\right\} \\ = & -\frac{\mathrm{i}\Gamma}{2\pi}\log\left\{C\frac{2h}{\pi}\frac{\sinh[\pi(z - z_n)/2h]}{\cosh[\pi(z - \tilde{z}_n)/2h]}\right\} \end{aligned} \tag{A.2}$$

where the tilde stands for the complex conjugate operator. The constant $C \equiv \prod_{k=1}^{\infty}[2k/(2k-1)]^2$ is irrelevant for the derivation of the velocity field and we can drop it from the velocity potential, together with the factor $2h/\pi$.

The self-induced velocity potential is obtained in a similar fashion, simply not accounting for the first contribution in Eq. (A.1). The self-induced velocity of a straight filament of vorticity is indeed null, so that the singular component of the complex potential at z_m can be discarded. We obtain

$$w_m(z_m) = -\frac{\mathrm{i}\Gamma}{2\pi}\log\left\{\frac{1}{\cosh[\pi(z_m - \tilde{z}_m)/2h]}\right\} \tag{A.3}$$

where the constant C has been dropped without affecting the velocity field.

The velocity of the vortex m, derived from the summation of the potentials $w(z_m) = w_m(z_m) + w_n(z_m)$, respectively, given by Eqs. (A.3) and (A.2), is

$$u_m - \mathrm{i}v_m = -\frac{\mathrm{i}\Gamma}{2\pi}\frac{\mathrm{d}}{\mathrm{d}z}\left\{\frac{\sinh[\pi(z - z_n)/2h]}{\cosh[\pi(z - \tilde{z}_n)/2h]\cosh[\pi(z - \tilde{z}_m)/2h]}\right\}_{z=z_m} \tag{A.4}$$

and we find the velocity components:

$$\begin{aligned} u_m = & -\frac{\Gamma}{4h}\left\{\frac{\sin[\pi(y_m - y_n)/h]}{\cosh[\pi(x_m - x_n)/h] - \cos[\pi(y_m - y_n)/h]} + \frac{\sin[\pi(y_m + y_n)/h]}{\cosh[\pi(x_m - x_n)/h] + \cos[\pi(y_m + y_n)/ht]}\right. \\ & \left. + \frac{\sin(2\pi y_m/h)}{1 + \cos(2\pi y_m/h)}\right\} \end{aligned} \tag{A.5}$$

$$v_m = -\frac{\Gamma}{4h}\left\{\frac{-\sinh[\pi(x_m - x_n)/h]}{\cosh[\pi(x_m - x_n)/h] - \cos[\pi(y_m - y_n)/h]} + \frac{\sinh[\pi(x_m - x_n)/h]}{\cosh[\pi(x_m - x_n)/h] + \cos[\pi(y_m + y_n)/h]}\right\} \tag{A.6}$$

Appendix B. Desingularization of the vortex filaments

The case of sound production by a two-dimensional spinning vortex pair is used for the validation of the numerical integration of Lighthill's desingularized volumetric source field (surface integral in two dimensions) by comparison with an analytical prediction. The desingularized vortices are sampled on a square field extending from -1 to 1 m in both x- and y-directions, with a uniform mesh spacing Δ equal to 0.01 m in both directions. The vortices have a circulation $\Gamma = 1\,\mathrm{m}^2\,\mathrm{s}^{-1}$, are separated by $d = 0.5\,\mathrm{m}$, and are spinning around the center of the sampled field with an angular velocity $\Omega = \Gamma/(\pi d^2)$ (see Fig. 18).

The reference pressure field is provided by Howe for the far-field pressure [12]:

$$p' \approx -4\sqrt{\frac{\pi d}{2r}}\rho_0 U^2 M^{3/2} \cos\left[2\theta - 2\Omega\left(t - \frac{r}{c_0}\right) + \frac{\pi}{4}\right] \tag{B.1}$$

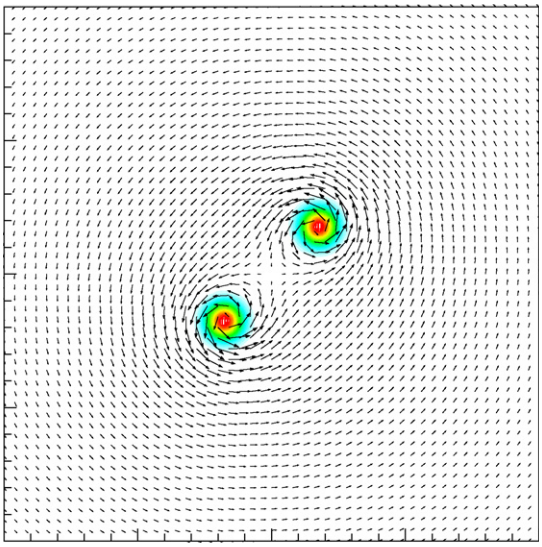

Fig. 18. Velocity and vorticity fields (every fourth vector is shown for clarity), $\sigma/d = 0.1$.

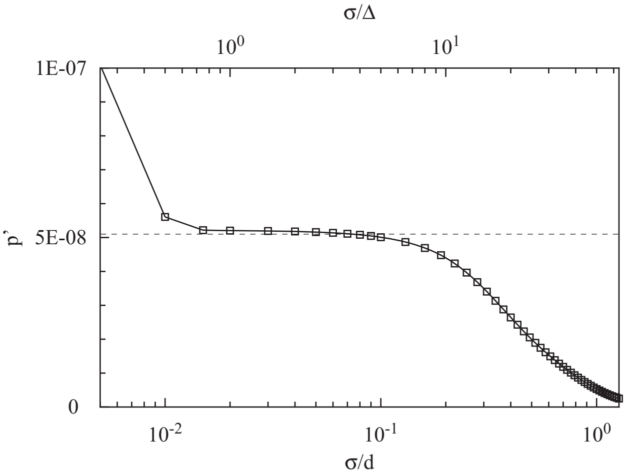

Fig. 19. Sound prediction based on numerical implementation of Lighthill's analogy and theoretical prediction.

where $U = \Omega d/2$ is the convection velocity of each filament, $M = U/c_0$ is the Mach number, and (r, θ) are the polar coordinates of the listener.

Fig. 19 shows the sound pressure field at the listener position $(r = 60\lambda, \theta = 0)$ integrated from the Lighthill source field, for a range of values of the desingularized core size σ. The dashed line indicates the reference far-field pressure (B.1). The results, shown for a frequency equal to Ω/π, highlight two different trends for small and large values of σ. For large values, the relevant non-dimensional parameter being σ/d, the integrated sound pressure drops to zero as the vorticity smears over the integration field. For small values, the integrated pressure rises sharply due to the increasing numerical noise when the vortex becomes under-resolved, around $\sigma/\Delta = 0.7$. In the region $0.7\Delta < \sigma < 0.1d$, the prediction follows a plateau, in fair agreement with the theoretical value for filament vortices. It was further observed that this agreement improves when the extent of the integration domain increases, for a constant value of σ/Δ. This is due to the truncation of the velocity field that is apparent in Fig. 18. On the basis of these results, a desingularization parameter $\sigma = 2\Delta = 0.02d$ has been used for the ducted spinning case.

References

[1] M.J. Lighthill, On sound generated aerodynamically. Part I. General theory, *Proceeding of the Royal Society of London A* 211 (1952) 564–587.

[2] N. Curle, The influence of solid boundaries upon aerodynamic sound, *Proceeding of the Royal Society of London A* 231 (1955) 505–514.

[3] H.G. Davies, J.E. Ffowcs Williams, Aerodynamic sound generation in a pipe, *Journal of Fluid Dynamics* 32 (4) (1968) 765–778.

[4] P.A. Nelson, C.L. Morfey, Aerodynamics sound production in low speed flow ducts, *Journal of Sound and Vibration* 79 (2) (1981) 263–289.

[5] M.C.A.M. Peters, A. Hirschberg, Acoustically induced periodic vortex shedding at sharp edged open channel ends: simple vortex models, *Journal of Sound and Vibration* 161 (2) (1993) 281–299.

[6] X. Gloerfelt, F. Pérot, C. Bailly, C. Juvé, Flow-induced cylinder noise formulated as a diffraction problem for low Mach numbers, *Journal of Sound and Vibration* 287 (2005) 129–151.

[7] C. Schram, J. Anthoine, A. Hirschberg, Calculation of sound scattering using Curle's analogy for non-compact bodies, *Proceedings of the 11th AIAA/CEAS Aeroacoustics Conference and Exhibit, number 2005-2836*, Monterey, CA, May 23–25, 2005.

[8] M.S. Howe, A. Winslow, M. Ikida, T. Fukuda, Rapid calculation of the compression wave generated by a train entering a tunnel with a vented hood: short hoods, *Journal of Sound and Vibration* 311 (2008) 254–268.

[9] O. von Estorff, *Boundary Elements in Acoustics*, WIT Press, 2000.

[10] T. Takaishi, M. Miyazawa, C. Kato, A computational method of evaluating noncompact sound based on vortex sound theory, *Journal of the Acoustical Society of America* 121 (3) (2007) 1353–1361.

[11] G.K. Batchelor, *An Introduction to Fluid Dynamics*, Cambridge University Press, Cambridge, 1967.

[12] M.S. Howe, *Theory of Vortex Sound, Cambridge Texts on Applied Mathematics*, Cambridge University Press, Cambridge, 2003.

[13] A. Hirschberg, C. Schram, A primitive approach in aeroacoustics, in: Y. Aurégan, A. Maurel, V. Pagneux, J.-F. Pinton (Eds.), *Lecture Notes in Physics*, Vol. 586, Springer, Berlin, Heidelberg, 2002, pp. 1–30.